PAPER

Check for updates

Ultrafast Channel II process induced by a 3-D texture with enhanced acceptor order ranges for high-performance non-fullerene polymer solar cells†

Shanshan Chen,‡[a] Sang Myeon Lee,‡[a] Jianqiu Xu,‡[b] Jungho Lee,‡[a] Kyu Cheol Lee,[ac] Tianyu Hou,[d] Yankang Yang,[e] Mingyu Jeong,[a] Byongkyu Lee,[a] Yongjoon Cho,[a] Sungwoo Jung,[a] Jiyeon Oh,[a] Zhi-Guo Zhang, [iD][e] Chunfeng Zhang,[b] Min Xiao,[b] Yongfang Li [iD][e] and Changduk Yang [iD] *[a]

To achieve efficient non-fullerene polymer solar cells (NF-PSCs), an in-depth understanding of the key properties that govern the power output is necessary. Herein, three trialkylsilyl substituted benzodithiophene-based polymer donors (PJ1, PJ2, and PJ3) were synthesized with fine-tuning of the highest occupied molecular orbital (HOMO)/lowest unoccupied molecular orbital (LUMO) and optical absorption. Using the polymer series paired with absorption-complementary small molecular acceptors (SMAs), namely, *m*-ITIC, IDIC, and AIDIC, we systematically studied the performance of a 3 × 3 matrix of NF-PSCs. An increasing open-circuit voltage with deepening HOMOs of the polymer donors, and the enhanced short-circuit current (J_{SC}) and fill factor (FF) were ascribed to the well-intermixed blend morphology containing enhanced SMA order ranges with mixed face-on and edge-on orientations, the so-called 3-D texture. Such an optimal microstructure is best exemplified in the PJ2:IDIC combination, affording a highest efficiency of 12.01% with a simultaneously high J_{SC} of 17.0 mA cm^{-2} and FF of 75.3%. The devices with an active layer thickness of 300 nm still maintain an impressive efficiency approaching 10% with a decent FF of 60.0%. Moreover, the Channel II process, *i.e.*, photoinduced hole transfer through acceptor excitation, was demonstrated to be crucially important for photocurrent generation. This study highlights the importance of optimizing the trade-off between charge separation/transport and domain size to achieve high-performance NF-PSCs.

Broader context

Solar cells, a renewable, clean energy technology that efficiently converts sunlight into electricity, are a promising long-term solution for energy and environmental problems caused by mass production and the use of fossil fuels. Recently, non-fullerene polymer solar cells (NF-PSCs) comprising p-type conjugated polymer donors and n-type non-fullerene small molecular acceptors (SMAs) have emerged as an encouraging photovoltaic technology due to distinguished advantages of low cost, synthetic flexibility, and easy tuning of absorption and electronic energy levels for both materials. In order to better understand the key parameters and mechanisms that govern NF-PSC performance, in this work, we have not only synthesized each donor polymer and acceptor series with absorption-complementary properties, but also investigated different combinations performance matrix of NF-PSCs. An optimized microstructure consisting of enhanced SMA order ranges in a well-intermixed 3-D textured blend resulted in a NF-PSC with superior efficiency. Moreover, our findings with regard to the transient absorption behavior demonstrated the vital role of the ultrafast Channel II process, *i.e.*, photoinduced hole transfer through acceptor excitation, for photocurrent generation in NF-PSCs, leading to new design and matching principles of organic conjugated materials for high-performance NF-PSCs.

[a] *Department of Energy Engineering, School of Energy and Chemical Engineering, Perovtronics Research Center, Low Dimensional Carbon Materials Center, Ulsan National Institute of Science and Technology (UNIST), 50 UNIST-gil, Ulju-gun, Ulsan 44919, South Korea. E-mail: yang@unist.ac.kr*

[b] *National Laboratory of Solid State Microstructures, School of Physics, and Collaborative Innovation Center of Advanced Microstructures, Nanjing University, Nanjing 210093, China*

[c] *Research Center for Green Fine Chemicals, Korea Research Institute of Chemical Technology, Ulsan 44412, South Korea*

[d] *Key Laboratory of Flexible Electronics (KLOFE) & Institute of Advanced Materials (IAM), Jiangsu National Synergetic Innovation Center for Advanced Materials (SICAM), Nanjing Tech University (NanjingTech), Nanjing 211816, China*

[e] *Beijing National Laboratory for Molecular Sciences, CAS Key Laboratory of Organic Solids, Institute of Chemistry, Chinese Academy of Sciences, Beijing 100190, China*

† Electronic supplementary information (ESI) available: Figures and tables. See DOI: 10.1039/c8ee01546e

‡ S. C., S. M. L., J. X., and J. L. contributed equally to this work.

Introduction

Non-fullerene small molecular acceptors (SMAs) are being extensively researched and have quickly become promising alternatives to the widely used fullerene acceptors for efficient bulk heterojunction (BHJ) non-fullerene polymer solar cell (NF-PSC) applications. Such SMAs have advantages including low cost, simple synthesis methods, and various structural adjustability for favorable absorption ranges and alignment of frontier energy levels.[1–24] Driven by the vast number of developed non-fullerene SMAs, power-conversion efficiencies (PCEs) over 11% have already been achieved in NF-PSCs,[2,3,6,13–15,17] and considerable efforts have been dedicated to understanding the important principles behind material matching, morphology control, and device physics. Such studies have provided valuable criteria for high-performance NF-PSCs, including: (i) appropriate donor and accepter combinations to complement the absorption in the visible and near-infrared regions, which can potentially increase the short-circuit current (J_{SC}); (ii) favorable matching of the frontier energy levels between the donor and acceptor likely resulting in a high open-circuit voltage (V_{OC}); and (iii) optimized blend morphology, degree of crystallinity, donor–acceptor phase separation, and domain sizes to simultaneously enhance the J_{SC} and fill factor (FF) values.[3,6,14,19,20,25–27,30–32,34–39]

Besides, photocurrent generation in BHJ PSCs can occur via (i) Channel I: donor excitation followed by electron transfer to the acceptor, related to the lowest unoccupied molecular orbital (LUMO) energy offset and (ii) Channel II: acceptor excitation followed by hole transfer to the donor, related to the highest occupied molecular orbital (HOMO) energy offset.[1,40–43] Photocurrent generation in PSCs based on fullerene acceptors predominantly occurs via Channel I due to their low optical absorptivity and hence, Channel II is often neglected. However, both mechanisms are relevant for NF-PSCs due to the strong absorbance of narrow band gap non-fullerene SMAs. Interestingly, there are multiple reports showing that NF-PSC systems with energy offsets less than the exciton binding energy (0.3 eV) can still function well, producing high PCEs exceeding 10%.[3,6,13–15,28,32,39,44] Therefore, the charge transfer dynamics, especially the Channel II mechanism, is currently being re-evaluated by the NF-PSC community.[32,45] However, despite the wide range of reported polymer donors and non-fullerene SMAs, a comprehensive study of the interplay between polymer donor and non-fullerene acceptor is still lacking. Hence, there is an urgent need to investigate the structure–property relationships related to NF-PSCs with systemically tuned frontier energy levels of both donor and acceptor materials.

With aiming at better understanding the key parameters and mechanisms that govern NF-PSC performance, in this work, we carried out a systemic study of a 3 × 3 NF-PSC matrix using a combination of three polymer donors and three SMAs. Motivated by the recently emerging positive effect of incorporating trialkylsilyl substituted benzodithiophene (BDTT-Si) into the polymer backbone on photovoltaic properties,[32,46] we decided to prepare BDTT-Si polymer analogs containing various electron-deficient building blocks to achieve optimized frontier energy levels and optical properties. When combined with relatively narrow band gap SMAs, namely, m-ITIC, IDIC, and AIDIC, the NF-PSCs showed a large variation of PCE in the range 2.06–12.01% subject to the donor–acceptor combinations. We found that the well-intermixed blend morphology containing an enhanced SMA order range along with the formation of a 3-D texture (mixed face-on and edge-on orientations) resulted in superior device performance of over 12% PCE for the PJ2:IDIC combination. High tolerance of the active layer thickness was demonstrated with a PCE approaching 10% even at the thickness of 300 nm. Moreover, our findings with regard to the observed J_{SC} and transient absorption behavior demonstrated the vital role of the ultrafast Channel II process for photocurrent generation in the NF-PSCs, leading to new design and matching principles of organic conjugated materials for high-performance NF-PSCs.

Results and discussion

Material design and properties

A series of BDTT-Si-based polymer donors (Fig. 1a) was synthesized through Pd-mediated Stille coupling polymerization of bis-stannylated BDTT-Si (M1)[32] with either dibrominated thienopyrroledione (TPD, M2),[63] benzodithiophenedione (BDD, M3),[33] or difluorobenzothiadiazole (DFBT, M4)[56] electron-deficient co-monomers, which are denoted as PJ1, PJ2, and PJ3, respectively. Detailed synthesis procedures and characterization are given in the Experimental section. All the polymer donors had similar high number-average molecular weights of ∼80 kDa, as determined by gel permeation chromatography at 120 °C, and sufficient solubility in common organic solvents.

As shown in Fig. 1b, the thin film absorption spectra exhibited a clear dependence on the electron-deficient moieties neighboring BDTT-Si along the polymer backbone, showing red shifts in the order PJ1 < PJ2 < PJ3, which corresponds to their increasing electron-accepting strength. Considering the complementary absorption profiles with the polymer donors, three SMAs (m-ITIC, IDIC, and AIDIC) were chosen, where the new AIDIC with n-hexyl side chains was prepared using a slightly modified synthesis method.[47] The film absorption spectra of m-ITIC and IDIC were very similar, both showing red-shifted absorption compared to AIDIC, due to the increased π-conjugation length and co-planarity in the backbones. The optical bandgaps (E_g^{opt}) of each polymer donor and small acceptor series, estimated from the film absorption edges, were 2.00, 1.81, and 1.75 eV for PJ1, PJ2, and PJ3, respectively and 1.59, 1.57, and 1.69 eV for m-ITIC, IDIC, and AIDIC, respectively. Moreover, the maximum absorption coefficient of the donor polymers films increased gradually in the following order: PJ2 (5.5×10^4 cm^{-1}), PJ3 (6.3×10^4 cm^{-1}), and PJ1 (7.1×10^4 cm^{-1}), while the three SMA films exhibited comparable values (Fig. S2, ESI†).

Ultraviolet photoelectron spectroscopy (UPS) was employed to evaluate the HOMO levels of the polymer donors and SMAs (Fig. S3, ESI†), where the LUMO levels were calculated from $E_{LUMO} = E_{HOMO} + E_g^{opt}$. The energy band alignment is illustrated in Fig. 1c. For the polymer donor series, the LUMOs were similar and in the range −3.26 to −3.38 eV, while the HOMOs
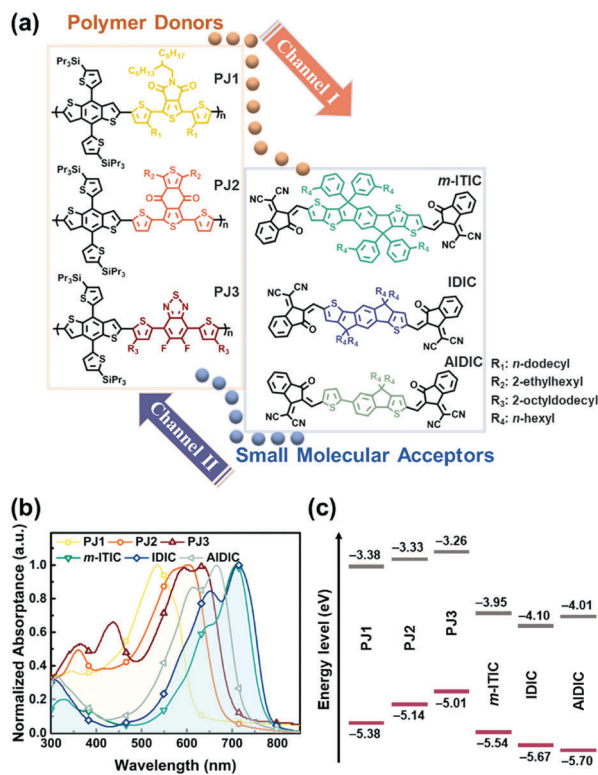
Fig. 1 (a) Chemical structures of polymer donors and small molecular acceptors used in this work. (b) Optical absorption spectra of neat films. (c) The UPS-derived energy level diagram.

Fig. 2 (a) The J–V curves. (b) EQE spectra and (c) corresponding integrated J_{SC}. (d) Comparative graph of J_{SC}, V_{OC}, FF, and PCE parameters for NF-PSCs: (i) PJ1:m-ITIC, (ii) PJ1:IDIC, (iii) PJ1:AIDIC, (iv) PJ2:m-ITIC, (v) PJ2:IDIC, (vi) PJ2:AIDIC, (vii) PJ3:m-ITIC, (viii) PJ3:IDIC, and (ix) PJ3:AIDIC.

gradually up-shifted, −5.38 eV, −5.14 eV, and −5.01 eV for PJ1, PJ2, and PJ3, respectively. Structurally, PJ1, PJ2, and PJ3 differ only in the acceptor conjugated with the BDTT-Si unit. Therefore, we can reasonably speculate that the electron-accepting strength of the moiety neighboring BDTT-Si along the polymer backbone was in the order TPD < BDD < DFBT. However, for the SMA series, the HOMO and LUMO values varied from −5.54 to −5.70 eV and from −3.95 to −4.10 eV, respectively. In all cases, the LUMO energy offsets were larger than the exciton binding energy, which ensures efficient photoinduced electron transfer, while the HOMO energy offsets changed from −0.16 to −0.32 eV, −0.4 to −0.56 eV, and −0.53 to −0.69 eV for PJ1, PJ2, and P3, respectively, within the given acceptor series. Note that either the cyclic voltammetry (CV) – or density functional theory (DFT) calculations – derived HOMO and LUMO energies somewhat deviate from UPS results but retain a similar trend (Fig. S4 and S5, ESI†).

Photovoltaic properties

The photovoltaic properties of all possible combinations of polymer donors and SMAs in the 3 × 3 device matrix were investigated using a conventional NF-PSC configuration ITO/PEDOT:PSS/active layer/PDINO/Al, where ITO, PEDOT:PSS, and PDINO refer to indium tin oxide, poly(3,4-ethylenedioxythiophene):poly(styrene sulfonate), and perylene diimide functionalized with amino N-oxide,[48] respectively. Independent device optimization was undertaken by carefully screening the donor/acceptor ratios, amount of 1,8-diiodooctane (DIO) additive, and annealing temperature
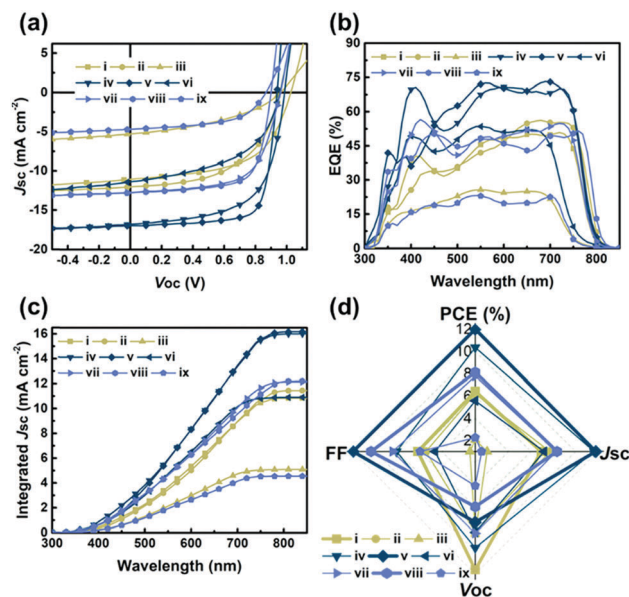
(Tables S6–S14, ESI†). Fig. 2a shows the representative curves of current density versus voltage (J–V) measured under AM 1.5G simulated solar spectrum conditions at 100 W cm^{-2}; the relevant photovoltaic parameters are summarized in Table 1. Fig. 2b and c display the corresponding external quantum efficiency (EQE) spectra and corresponding integrated J_{SC} values, respectively, which are consistent with the J_{SC} values obtained from J–V measurements (within 5% mismatch). As a result of its deeper HOMO level, the PJ1-based devices show superior V_{OC} values of 0.961–1.031 V; however, both the J_{SC} and FF values overall lay far behind the other two polymer donor-based ones. A high J_{SC} is generally related to an extension of the absorption range as well as the absorption coefficient.[13,14,29,49–53] However, the J_{SC} values of the devices fabricated from the given SMAs showed a nonlinear dependence on the absorption behavior of the donor polymers; PJ2-derived devices showed J_{SC}s of 11.4–17.0 mA cm^{-2}, higher than both the PJ1 and PJ3 cases with similar J_{SC}s ≈ 5–12 mA cm^{-2}. In contrast, for a given polymer donor series, the J_{SC} values show a clear linear dependence on the red-shifted absorption width of the SMAs in the following order: AIDIC < m-ITIC < IDIC. These results demonstrate that the Channel II-type mechanism is a major factor contributing to the increased J_{SC} values of the NF-PSCs studied here.[1]

On the other hand, comparing the devices based on the different SMAs with the same polymer donor revealed that V_{OC} was not proportional to the relative LUMO levels of the SMAs, where higher V_{OC} values were observed for m-ITIC-based devices than the others. In addition, compared with the AIDIC-based devices, both m-ITIC- and IDIC-based ones exhibited significantly improved J_{SC} and FF values, especially for PJ2 combinations. Among all tested devices, the best PCE of 12.01% was

Table 1 Photovoltaic parameters of the NF-PSCs under the illumination AM 1.5G, 100 mW cm^{-2}

Devices	V_{OC}^{a} (V)	J_{SC}^{a} (mA cm^{-2})	FF^{a} (%)	PCE^{a} (%)	R_s^{b} (Ω cm^{-2})	R_{sh}^{c} (kΩ cm^{-2})	J_{SC}^{d} (mA cm^{-2})	Thickness^{a} (nm)
PJ1:*m*-ITIC	1.031 (1.030 ± 0.004)	11.1 (11.1 ± 0.2)	56.0 (55.4 ± 1.1)	6.41 (6.31 ± 0.14)	11.43 (11.85 ± 0.60)	0.63 (0.62 ± 0.07)	10.9	110.9 ± 2.2
PJ1:IDIC	0.958 (0.955 ± 0.003)	12.0 (11.9 ± 0.3)	53.6 (53.1 ± 0.9)	6.18 (6.05 ± 0.16)	11.00 (11.29 ± 0.54)	0.60 (0.60 ± 0.05)	11.5	109.1 ± 2.4
PJ1:AIDIC	0.961 (0.960 ± 0.005)	5.9 (5.3 ± 0.2)	40.6 (39.5 ± 1.1)	2.06 (1.95 ± 0.09)	54.03 (53.27 ± 0.83)	0.37 (0.38 ± 0.04)	5.1	115.4 ± 1.9
PJ2:*m*-ITIC	0.988 (0.987 ± 0.002)	16.8 (16.7 ± 0.2)	62.3 (62.0 ± 0.9)	10.34 (10.19 ± 0.15)	7.67 (7.91 ± 0.62)	1.16 (1.08 ± 0.06)	16.0	112.6 ± 3.3
PJ2:IDIC	0.939 (0.935 ± 0.005)	17.0 (16.9 ± 0.2)	75.3 (74.9 ± 0.7)	12.01 (11.83 ± 0.14)	6.05 (6.32 ± 0.51)	1.70 (1.66 ± 0.05)	16.2	110.3 ± 2.9
PJ2:AIDIC	0.958 (0.954 ± 0.004)	11.4 (11.2 ± 0.2)	50.9 (50.0 ± 1.1)	5.56 (5.43 ± 0.15)	12.33 (12.78 ± 0.90)	0.50 (0.54 ± 0.06)	10.9	119.1 ± 2.1
PJ3:*m*-ITIC	0.960 (0.962 ± 0.003)	12.7 (12.6 ± 0.2)	63.5 (62.8 ± 0.7)	7.76 (7.45 ± 0.19)	10.88 (10.88 ± 0.75)	1.02 (1.01 ± 0.04)	12.1	117.8 ± 3.1
PJ3:IDIC	0.908 (0.902 ± 0.005)	12.8 (12.7 ± 0.2)	69.8 (69.1 ± 0.9)	8.11 (7.93 ± 0.20)	10.04 (10.63 ± 0.82)	1.19 (1.15 ± 0.04)	12.2	114.5 ± 2.7
PJ3:AIDIC	0.867 (0.870 ± 0.004)	4.7 (4.6 ± 0.2)	55.4 (54.7 ± 1.2)	2.25 (2.10 ± 0.12)	55.49 (55.03 ± 0.95)	0.47 (0.45 ± 0.04)	4.5	120.7 ± 3.2

^{a} The average values are obtained from 15 devices, with the standard deviation. ^{b} The average values are obtained from the inverse slope at $V = V_{OC}$ in J–V curves under illumination, with the standard deviation. ^{c} The average values are obtained from the inverse slope at $V = 0$ in J–V curves under illumination, with the standard deviation. ^{d} The short-circuit current densities are integrated from the EQE spectra.

achieved for the PJ2:IDIC combination with the highest J_{SC} of 17.0 mA cm^{-2} and FF of 75.3%, and a moderate V_{OC} of 0.939 V, whereas the PJ1:ADIC-derived device showed the lowest PCE of 2.06%. It is worth noting that the achieved FF is one of the highest values reported for NF-PSCs to date. The complicated behavior of the J_{SC}, V_{OC}, FF, and PCE values is shown using a radar chart (Fig. 2d). It can be seen that many factors in addition to favorable absorption properties and energy level alignment critically contribute to photovoltaic performance, and these factors are discussed in the following sections.

Moreover, the effect of active layer thickness on the photovoltaic performance of the best-performing PJ2:IDIC couple was investigated (Table S1 and Fig S6, ESI†). It was noted that even at an active layer thickness of 300 nm, the PJ2:IDIC device can still afford an impressive PCE close to 10% with a decent FF of 60.0%. The excellent and thickness-insensitive properties of the NF-PSC based on PJ2:IDIC makes it a promising candidate for large scale fabrication.

Morphological characterization

Grazing incidence wide-angle X-ray scattering (GIWAXS) measurements were conducted to define the molecular-scale packing and orientational texture of the neat polymer donors, SMAs, and blend films (Fig. 3a). Both the neat donor and acceptor
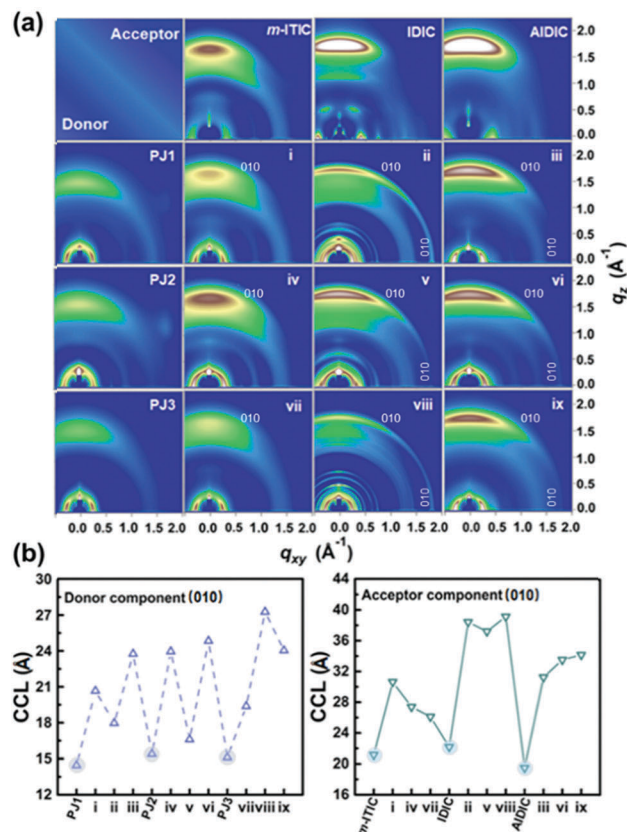

Fig. 3 (a) GIWAXS images of the neat and blend films: (i) PJ1:*m*-ITIC, (ii) PJ1:IDIC, (iii) PJ1:AIDIC, (iv) PJ2:*m*-ITIC, (v) PJ2:IDIC, (vi) PJ2:AIDIC, (vii) PJ3:*m*-ITIC, (viii) PJ3:IDIC, and (ix) PJ3:AIDIC; and (b) corresponding donor and acceptor component CCLs estimated from the face-on (010) diffractions.

samples in the first column and row of the 4 × 4 matrix exhibited (010) diffraction peaks along the out-of-plane direction, indicating the preferential π-face-on oriented stacking relative to the substrate. It is also worth noting that the neat donor films displayed a rather isotropic (100) lamellar peak in both out-of-plane and in-plane directions, whereas the neat SMA films showed a series of anisotropic multiple diffractions (especially for IDIC), indicating highly oriented polycrystalline structures. Likewise, for all blend films, the (010) π-face-on diffractions were observed. In particular, in addition to the occurrence of arc-like multiple peaks, the IDIC-based blend films showed a much sharper (010) pattern, suggesting significantly enhanced crystallinity. Besides, the (010) peaks in the in-plane line cuts appeared to some extent in the blend films, excluding m-ITIC-based samples (Fig. S8, ESI†), verifying the formation of mixed edge-on and face-on arrangements.

This 3-D texture is known to facilitate the coexistence of both vertical and parallel charge transport pathways in the active layer, leading to efficient charge carrier transfer and ultimately high FF of the device.[54,55] We also compared the (010) π-stacking crystallite coherence lengths (CCL_{010}) using the Scherrer equation,[40] where a clear difference between the (010) peak positions of the polymer donors ($\sim 1.60 \text{ Å}^{-1}$) and small acceptors ($\sim 1.80 \text{ Å}^{-1}$) enabled us to determine the corresponding (010) π-face-on peaks induced by each of the components in the blend films via multiple-peak fitting (Fig S9, ESI†). As shown in Fig. 3b, the neat polymer donors showed similar CCL_{010} values (in the range 14.45–15.39 Å), while the neat SMAs showed a gradual decline in the CCL_{010} from 22.18 Å for IDIC to 21.16 Å for m-ITIC to 19.49 Å for AIDIC, indicating IDIC had the largest crystallites. When blended with the polymer donors, the IDIC-based blend films exhibited much higher CCL_{010} values for IDIC (37.19–39.17 Å) than the other acceptor-based ones. In contrast, comparing each polymer donor series, we found relatively smaller CCL_{010} values for the polymer donor peaks in IDIC-containing samples, except for PJ3 systems. Hence, we conclude that the IDIC-containing blends retained high order ranges of IDIC, but showed relatively low polymer donor ordering, except for the PJ3 systems. The trade-off between the crystallinity of the polymer donor and SMA should directly correlate with device performance following the charge separation and transport properties.[39,56]

In addition, the best-performing PJ2:IDIC combination showed relatively smaller CCL_{010} values of the (010) peaks (considering both components), implying better intermixing of P2 and IDIC; this was considered one of the contributing factors to the observed highest PCE. Such desirable intermixing was further evidenced by contact angle measurements of each component (Fig. S10, ESI†).[57,58] IDIC showed lower interfacial tension (γ) with the polymer donor series compared with the other combinations, where the smallest γ of 0.24 mN m^{-1} was achieved for PJ2:IDIC (Table S3, ESI†). The bulk morphology of the blend films was further characterized using scanning transmission electron microscopy (STEM). As shown in Fig. 4, despite the lack of clear morphological trends with the varied polymer donor and SMA structures, for the given PJ2 set, the STEM images of both PJ2:m-ITIC and PJ2:IDIC films (Fig. 4,
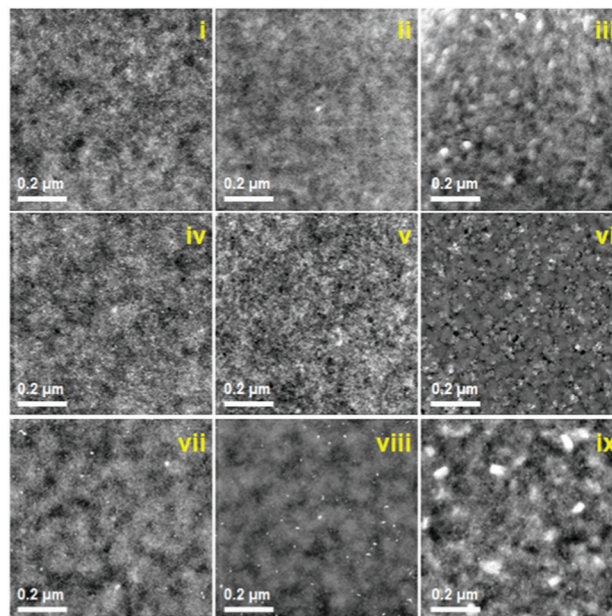

Fig. 4 STEM images of the blend films: (i) PJ1:m-ITIC, (ii) PJ1:IDIC, (iii) PJ1:AIDIC, (iv) PJ2:m-ITIC, (v) PJ2:IDIC, (vi) PJ2:AIDIC, (vii) PJ3:m-ITIC, (viii) PJ3:IDIC, and (ix) PJ3:AIDIC.

images iv and v) showed nanoscale phase-separated regions with interpenetrated networks. In particular, a clearly defined, fibril-like microstructure with fine domain sizes of ∼10–20 nm was observed for the PJ2:IDIC film. Smaller domain sizes result in a greater interfacial area between donor and acceptor, enabling more efficient dissociation of excitons into free carriers, consistent with the superior J_{SC} of the PJ2:IDIC device.[25,59–62] On the other hand, in the AIDIC-based films (Fig. 4, the third column), granular aggregates with poorly connected pathways are visible; the finite two-phase interface and large grain boundaries acted as a trap or barrier for charge splitting and transport, explaining the lower J_{SC} and FF of devices based on these materials.[20,56,63,64] The substantial differences in the surface roughness of the blends, measured using atomic force spectroscopy (AFM) (Fig. S11 and S12, ESI†), further demonstrated the dependence of the phase segregation on the blend composition (consistent with the STEM results). Collectively, one can speculate that achieving higher order ranges of SMAs and the observed 3-D textured structure within the well-intermixed blending system help realize simultaneously high J_{SC} and FF values in NF-PSCs.

Charge generation, dissociation, and transport properties

To directly compare the vertical charge carrier mobility of the blends, space charge limited current measurements were performed (Fig. S14, ESI†).[63–65] The hole mobilities, μ_hs, (4.11×10^{-5}–2.03×10^{-4} cm^2 V^{-1} s^{-1}) were generally 1.2–4.0 times larger than the corresponding electron mobilities, μ_es, (1.05×10^{-5}–1.61×10^{-4} cm^2 V^{-1} s^{-1}) in the blends (Fig. 5a). It was clear that the increasing trends of μ_h values were the same as those of the μ_e values. Note also the IDIC-based systems exhibited simultaneously enhanced μ_h and μ_e values within a given polymer series.
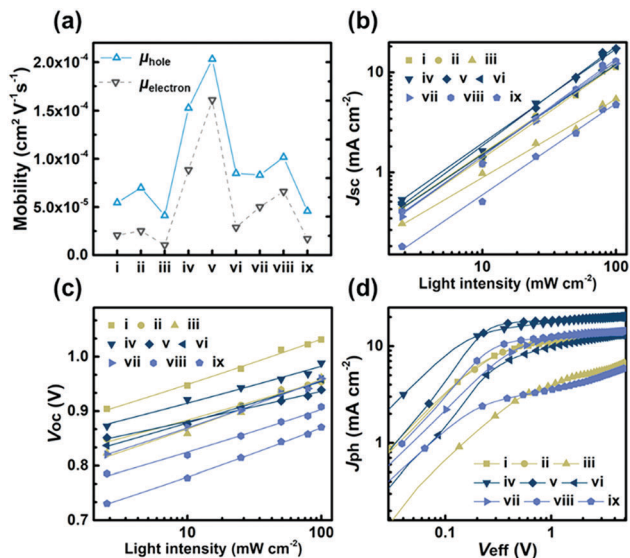
This journal is © The Royal Society of Chemistry 2018

Energy Environ. Sci., 2018, 11, 2569–2580 | 2573

Fig. 5 (a) The hole and electron mobilities. (b) J_{SC} as a function of light intensity and the corresponding α values are i (0.929), ii (0.927), iii (0.787), iv (0.943), v (0.994), vi (0.899), vii (0.946), viii (0.970), and ix (0.917), respectively. (c) V_{OC} as a function of light intensity and the corresponding slope values are i ($1.404kT/q$), ii ($1.297kT/q$), iii ($1.674kT/q$), iv ($1.196kT/q$), v ($1.020kT/q$), vi ($1.388kT/q$), vii ($1.598kT/q$), viii ($1.511kT/q$), and ix ($1.828kT/q$), respectively. (d) J_{ph} versus V_{eff} characteristics of the various donor and acceptor combinations: (i) PJ1:m-ITIC, (ii) PJ1:IDIC, (iii) PJ1:AIDIC, (iv) PJ2:m-ITIC, (v) PJ2:IDIC, (vi) PJ2:AIDIC, (vii) PJ3:m-ITIC, (viii) PJ3:IDIC, and (ix) PJ3:AIDIC.

The highest μ_h and μ_e values with the most balanced μ_h/μ_e ratio of 1.26 were observed for the best-performing PJ2:IDIC combination; this can reduce the accumulation of space charges and enhance J_{SC} and FF values.

Next, we analyzed the incident light intensity (I)-dependent J–V characteristics to elucidate the charge recombination kinetics in NF-PSCs. In general, J_{SC} can scale with a power-law dependence on I, $J_{SC} \propto I^\alpha$, where the exponent $\alpha = 1$ when bimolecular recombination is negligible under short-circuit conditions.[66] Within the given polymer donor sets, IDIC-based cells yielded higher α values (>0.900), where the value closest to unity ($\alpha = 0.994$) was observed for PJ2:IDIC (Fig. 5b). This suggests that the bimolecular recombination loss is least involved in the PJ2:IDIC blend, which agrees well with its highest carrier mobilities and FF performing in the device. Besides, either geminate or Shockley–Read–Hall recombination was evaluated via the semi-logarithmic scaling of V_{OC} versus I,[66] revealing a strong dependence of V_{OC} on I (Fig. 5c). The fitted data for IDIC-derived cells showed smaller slopes (the smallest slope of $1.020kT/q$ was observed for PJ2:IDIC) than the other samples, where k is Boltzmann's constant, T is temperature, and q is the elementary charge. These values reflect the weakest geminate recombination in the PJ2:IDIC system, probably related to the enhanced donor–acceptor interfacial area, which accounts for its excellent J_{SC}.

Additionally, the probabilities for exciton dissociation and charge collection in the devices were also extracted through plotting the net photocurrent (J_{ph}) as a function of effective

applied voltage (V_{eff}) (Fig. 5d). Here, J_{ph} is given by $J_{ph} = J_L - J_D$, where J_L and J_D are the photocurrent densities under illumination and in the dark, respectively; V_{eff} is given by $V_{eff} = V_0 - V_a$, where V_0 is the compensation voltage at $J_{ph} = 0$ and V_a is the applied bias voltage.[67] It was clear that J_{ph} became saturated (J_{sat}) at a high V_{eff} (>1.5 V) for all cases, except for PJ1:AIDIC and PJ3:AIDIC. This implies that a higher electric field is required for sweeping out all the charge carriers and separating the geminate electron–hole pairs in the PJ1:AIDIC and PJ3:AIDIC blends. Here, $P(E,T)$ is defined as the J_{ph}/J_{sat} ratio. Under short-circuit conditions, both the PJ2:m-ITIC and PJ2:IDIC cells exhibited comparatively higher $P(E,T)$ values (91.7% and 94.1%, respectively) than the other combinations (78.285.9%) (Table S4, ESI†). This suggests that the well-intermixed microstructure with nanoscale phase separation facilitates efficient exciton dissociation at the donor–acceptor interface. This is consistent with their significantly reduced geminate recombination loss and explains the outstanding J_{SC} values observed in PJ2:m-ITIC and PJ2:IDIC cells. Notably, maximizing the power output resulted in a sharp decrease in $P(E,T)$ values, while retaining a moderate $P(E,T)$ value of 79.3% in the PJ2:IDIC cell (Table S4, ESI†), indicating its outstanding charge extraction and collection efficiency.

Considering all these results, the charge transport and recombination properties were able to elucidate the fundamental mechanistic connection between blend microstructure and device performance. For example, precise control over conflicting crystallite characteristics between the polymer donor and SMA in the 3-D textured structure is favorable for simultaneously enhancing μ_h and μ_e, accompanied by reduced bimolecular recombination and thus, high FF values. This observation is generally associated with the relatively larger shunt resistance (R_{sh}) and smaller series resistance (R_s) values in the devices. The R_{sh} and R_s values of the best-performing PJ2:IDIC combination are 1.70 kΩ cm^{-2} and 6.05 Ω cm^{-2}, respectively, suggesting the better overall diode characteristics induced by the optimal BHJ morphology. At the same time, a well-intermixing blend microstructure promoted exciton dissociation with suppressed geminate recombination, leading to increased device J_{SC} values. Conclusively, by virtue of the well-mixed, interpenetrating 3-D texture with improved SMA order ranges, an optimal trade-off between charge separation and transport was realized in the best-performing PJ2:IDIC combination, yielding simultaneously high J_{SC} and FF values.

Photophysics

To gain further insight into the observed dominant Channel II mechanism for photocurrent generation, transient absorption (TA) spectroscopy measurements were performed on the high-performance PJ2-based system (Fig. 6). Since the primary absorption positions of the PJ2 polymer donor and SMA materials were well separated, selective excitation of each component can be allowed; pump wavelengths of 500 nm and 740 nm were chosen to excite the PJ2 and SMAs, respectively. The bleach signals at 720, 730, and 690 nm appeared in both the neat SMA and blend films, which was intrinsically ascribed to the ground state bleaching (GSB) of the transitions in m-ITIC, IDIC, and AIDIC, respectively.
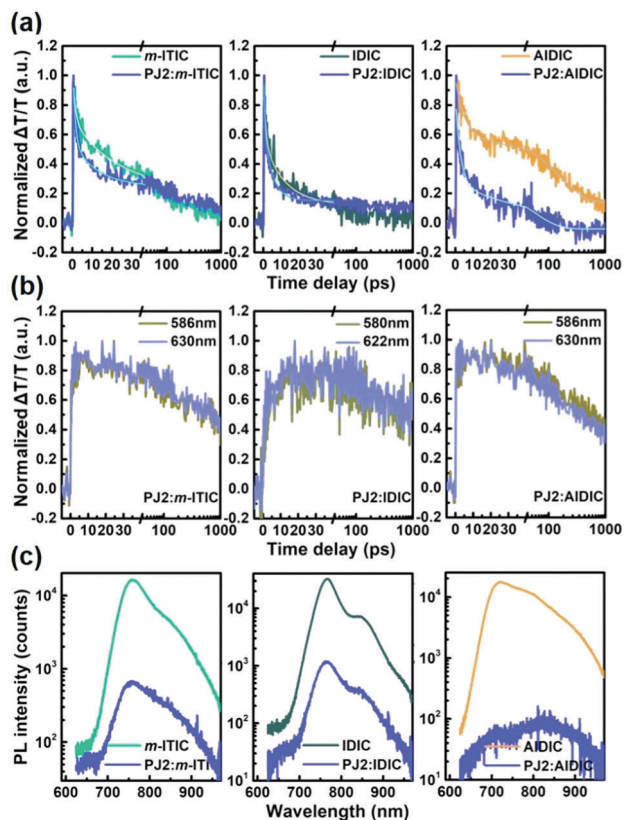
Fig. 6 (a) Transient absorption (TA) dynamics recorded from neat acceptors and corresponding blend films with the pump at 740 nm (m-ITIC and PJ2: m-ITIC films probed at 730 nm, IDIC and PJ2:IDIC films probed at 720 nm, AIDIC and PJ2:AIDIC films probed at 690 nm). (b) Transient absorption (TA) dynamics recorded from the blend films with the pump at 740 nm. (c) Photoluminescence spectra (PL) of neat acceptors and corresponding blend films, excited at 375 nm.

On the other hand, the additional bleach signals arising at around 586 and 630 nm corresponded with the GSB of PJ2 recorded under pumping at 500 nm. As shown in Fig. S15 in the ESI,† the bleaching signals of PJ2 were built with the decay of the bleaching signals of the SMAs in the tested blends, clearly evidencing photoexcited holes being transferred from the acceptor to donor, namely, the Channel II pathway.

In addition, it was found that at the early stage (<40 ps), the relaxation rates become significantly faster in the blends compared to the neat components. Also, the lifetime parameters of the blends, estimated by the bi-exponential decay function, exhibited the following order: PJ2:IDIC (0.42 ps, 4.93 ps) < PJ2:m-ITIC (1.22 ps, 12.62 ps) < PJ2:AIDIC (2.86 ps, 56.23 ps). This confirms that the most efficient hole transfer process was obtained in the PJ2:IDIC case, presumably the key factor for achieving its superior performance in the NF-PSCs tested here. Note that the GSB bleach signals in the PJ2:IDIC blend persisted for a longer time than those of the other blends (Fig. S16, ESI†), implying the existence of long-lived polarons, favorable for effective charge generation in the device.[41,68,69] Besides, photoluminescence (PL) quenching experiment was carried out to further verify the above-mentioned Channel II process

in the blends. Fig. 6c shows that the PL emissions of SMAs were dramatically quenched in the corresponding blend films, indicating that the effective hole transfer process occurs at the polymer donor:SMA interfaces.

To further substantiate the influence of the molecular ordering of the non-fullerene acceptor on the Channel II process and ultimately device performance, two high-performance thieno[2′,3′:5′,6′]-pyrido[3,4-g]thieno[3,2-c]isoquinoline-5,11(4H,10H)-dione-based polymer donors (PTPTI-T100 and PTPTI-T70)[39,70] were selected and paired with poly((N,N′-bis(2-octyldodecyl)-naphthalene-1,4,5,8-bis(dicarboximide)-2,6-diyl)-alt-5,5′-(2,2′-bithiophene)) (P(NDI2OD-T2))[62] and its fluorinated analogue (P(NDI2OD-T2F)) for a 2×2 all-polymer solar cell (all-PSC) characterization/performance optimization matrix (Fig. S18, ESI†). The all-PSCs based on PTPTI-T70 showed overall higher PCEs compared to the corresponding PTPTI-T100 ones (Fig. S19 and Table S5, ESI†), mainly due to the enhanced intermixing feature with finer donor–acceptor phase separation in the blends (Fig. S20, ESI†). In this series, the best performance was achieved with the PTPTI-T70:P(NDI2OD-T2F) combination, showing distinctly higher ordered characteristics of the acceptor component with relatively lower ordering of the donor component in a well-mixed, interpenetrating 3-D texture (Fig. S21 and S22, ESI†).

We also characterized the Channel II process of the PTPTI-T70-based all-PSCs by using TA measurement with a pump wavelength of 710 nm (Fig. S23 and S24, ESI†). From the kinetic curves probed at 633 nm, it is found that the rising lifetime ascribed to the donor component GSB signal in the PTPTI-T70:P(NDI2OD-T2F) blend ($\sim$0.79 ps) at the early stage was shorter than that of the PTPTI-T70:P(NDI2OD-T2) one ($\sim$0.87 ps), indicating that the transfer kinetics of the hole carriers is faster. This result is not only responsible for the relatively better performance in PTPTI-T70:P(NDI2OD-T2F), but also agrees well with the general trend observed in the PJ2:SMA systems. Moreover, the mono-exponential fitted lifetimes of the bleaching signal are 80 ns for the PTPTI-T70:P(NDI2OD-T2F) blend and 1.69 ns for the PTPTI-T70:P(NDI2OD-T2) blend, respectively, suggesting greatly reduced charge recombination in the optimal microstructures of the PTPTI-T70:P(NDI2OD-T2F) blend.

Stability

In addition to the improvement of the PCE, device stability is another key issue for the practical application of NF-PSCs. Fig. 7a shows the data for assessing the effect of thermal treatment on the best-performing PJ2:IDIC combination, where the devices were examined at various temperatures (ranging from 100 to 250 °C) for 5 min in an inert atmosphere. Some decreases of the photovoltaic performance were observed under heating up to 210 °C. Specifically, the PCE retained $\sim$90% of the initial value upon annealing at 170 °C and the device still showed a PCE as high as 9.02% ($\sim$75% of the initial value), even after annealing at 210 °C. However, the PCE declined sharply at further elevated temperature (250 °C). To gain insight into the effect of thermal stress on the photovoltaic performance, an investigation of the blend film microstructure and photophysics under various thermal treatment conditions (170, 210, and 250 °C)
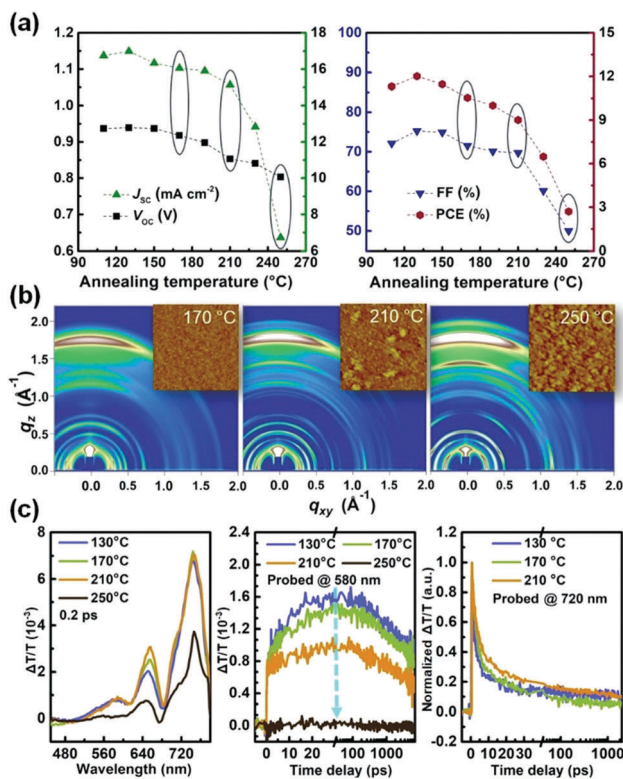
Fig. 7 (a) Device stability of the PJ2:IDIC based NF-PSCs exposed to different temperatures. (b) GIWAXS images of the PJ2:IDIC blend films exposed to 170, 210, and 250 °C, respectively. Insets: The corresponding AFM height images (root-mean square roughness: 1.67 nm (130 °C), 5.22 nm (210 °C), and 6.55 nm (250 °C)). (c) Transient absorption (TA) dynamics probed at 580 nm and 720 nm recorded from the PJ2:IDIC blend films exposed to different temperatures (130, 170, 210, and 250 °C).

was carried out. As shown in Fig. 7b, with increasing the annealing temperatures, the intensity of anisotropic multiple diffractions was significantly enhanced in the GIWAXS patterns, suggesting a higher crystalline order in the blend film. This is further evidenced from the comparisons of the CCL_{010} (Fig. S25, ESI†) and the surface roughness values (Fig. 7b) Nonetheless, thermally-induced coarse phase separation with larger aggregates occurred in the blend at the elevated temperatures, and became most grievous when processed at 250 °C (Fig. S26, ESI†), which is detrimental for the exciton dissociation and charge transfer in devices. Consequently, the maximum of the PJ2 bleaching signals ascribed to the hole transfer process gradually decreased as the annealing temperature increased, and eventually vanished in the blend film treated at 250 °C (Fig. 7c). The corresponding rising time of the PJ2 bleach signal in blends at the early stage, estimated using a mono-exponential decay function, revealed the following order: 130 °C (9.09 ps) < 170 °C (10.88 ps) < 210 °C (18.88 ps). Meanwhile, the decay lifetime of the IDIC bleach signal in blends at the early stage, estimated using a bi-exponential decay function, exhibited the same order: 130 °C (0.42 ps, 4.93 ps) < 170 °C (1.70 ps, 11.39 ps) < 210 °C (1.85 ps, 7.44 ps). These results indicate that thermally-induced large aggregate formation can strongly inhibit the hole transfer process, leading to poor photovoltage performance in NF-PSCs.

In addition, the long-term stability of the PJ2:IDIC-based device was also examined at room temperature in an inert atmosphere without encapsulation (Fig. S27, ESI†). The PJ2:IDIC-based device exhibited excellent stability with ~95% of its initial PCE after 45 days. It is found that the CCL_{010} value of IDIC shows a relatively larger reduction compared to the change of PJ2 in the blend after 45 days. Note also that the kinetics of the lifetime at the early stage (0.62 ps, 4.97 ps) is slower than that of the initial one, implying a less efficient hole transfer process, which likely accounts for the decreased device performance.

Conclusions

In summary, we have synthesized a series of polymer donors based on the BDTT-Si unit (PJ1, PJ2, and PJ3) and varied the HOMO and LUMO energy levels and optical properties via the introduction of various electron-deficient moieties (TPD, BDD, and DFBT) into the polymer backbones. The resulting polymer donors were combined with three small acceptors (m-ITIC, IDIC, and AIDIC) with complementary absorption ranges to study a 3 × 3 performance matrix of NF-PSCs. Observed differences in the V_{OC} were largely related to the different HOMO levels of the polymer donors, while J_{SC} and FF highly depended on the crystallinity of the two components and the morphology of the blend films. An optimized microstructure consisting of enhanced SMA order ranges in a well-intermixed 3-D textured blend was the key factor for simultaneously increasing J_{SC} and FF in the NF-PSCs. The best measured performance was for the PJ2:IDIC combination, achieving a maximum PCE of 12.01% with a high J_{SC} of 17.0 mA cm^{-2} and an outstanding FF of 75.3%. The observed linear dependence of J_{SC} on the red-shifted absorption profiles of the SMAs, rather than that of the polymer donors, demonstrated the vital role of a Channel II mechanism for photocurrent generation in NF-PSCs. This ultrafast Channel II process in the best-performing PJ2:IDIC combination was verified using TA spectroscopy measurements. Moreover, the photovoltaic performance of the best performing PJ2:IDIC combination exhibits excellent thickness-insensitivity with a high PCE close to 10% even at the thickness 300 nm, which is conductive for the large scale fabrication of NF-PSCs. These findings present an opportunity to reconsider the underlying mechanisms and key contributors for achieving both efficient charge separation and transport for high-performance NF-PSCs.

Experimental

Materials and measurements

All the chemicals and reagents were purchased from Solarmer Energy Inc., Aldrich Co., Alfa Aesar, and TCI Co. without further purification. All solvents were ACS grade unless otherwise noted. (5,5′-(2,6-Bis(trimethylstannyl)benzo[1,2-b:4,5-b′]dithiophene-4,8-diyl)bis(thiophene-5,2-diyl))bis(tripropylsilane) (M1),[32] 1,3-bis[5-bromo-3-(n-dodecyl)thien-2-yl]-5-(2-hexyldecyl)thieno[3,4-c]pyrrole-4,6-dione (M2),[63] 1,3-bis(5-bromothiophen-2-yl)-5,7-bis(2-ethylhexyl)benzo[1,2-c:4,5-c′]dithiophene-4,8-dione (M3),[33] and

5,6-difluoro-4,7-bis[5-bromo-4-(2-octyldodecyl)thiophene-2-yl]-benzo[*c*][1,2,5]thiadiazole (M4)[56] were prepared according to the reported procedures. ^{1}H NMR spectra were measured using a Varian VNRS 400 MHz spectrometer using deuterated chloroform (CDCl$_3$) as a solvent and tetramethylsilane (TMS) as an internal reference. The elemental analysis of carbon (C), hydrogen (H), nitrogen (N) and sulfur (S) was recorded with a Flash 2000 elemental analyzer. The UV-visible spectra were measured using a UV-1800 (SHIMADZU) spectrometer. The ultraviolet photoelectron spectroscopy (UPS) measurements were made using an AXIS-NOVA CJ109, Kratos under a base pressure of 1.0×10^{-9} Torr with a He I photo source ($h\nu = 21.22$ eV). Cyclic voltammetry (CV) was performed using a Solartron electrochemical station (METEK, Versa STAT3) equipped with a three-electrode cell in tetra-*n*-butylammonium hexafluorophosphate solution in acetonitrile (0.1 M) at a scan rate of 50 mV s^{-1} under an argon atmosphere at room temperature. A Ag/Ag$^+$ electrode, a platinum wire and a glass carbon disk were used as the reference electrode, counter electrode and working electrode, respectively. The HOMO energy levels were obtained from the equation HOMO (eV) = $-(E_{(ox)}^{onset} - E_{(ferrocene)}^{onset} + 4.8)$. The LUMO levels of polymers were obtained from the equation LUMO (eV) = $-(E_{(red)}^{onset} - E_{(ferrocene)}^{onset} + 4.8)$. The theoretical calculations were performed using density functional theory (DFT) B3LYP with the 6-31G* basis set. The average number molecular weights (M_ns) and polydispersity index (PDI) of the present polymers were determined using high-temperature gel permeation chromatography (HT-GPC) with Agilent 1200 HPLC and mini-DAWN TREOS with the polystyrene standard in 1,2,4-trichlorobenzene at 120 °C. The contact angles of all the materials were obtained using the Phoenix 300 Model instrument. The transient absorption (TA) was performed using a regenerative amplifier (Libra, Coherent, 1 kHz, 90 fs) with tunable wavelength and analyzed using a high-speed charge-coupled device (S11071-1104, Hamamatsu) with a monochromater (Acton 2358, Princeton Instrument) at 1 kHz enabled by a custom-built board from Entwicklungsbuero Stressing. The angle between the polarizations of the pump and probe beam was set at the magic angle.

General procedure for synthesis and purification

The dibrominated monomer (M2, M3, or M4) (0.10 mmol) and bis-stannylated M1 (0.10 mmol) were taken in a long Schlenk tube under argon conditions with 3 mL anhydrous toluene and 1 mL *N,N*'-dimethylformamide. The mixture was degassed for 10 min, followed by addition of a solution of Pd(PPh$_3$)$_4$ (2.0 μmol) in 1 mL toluene to the tube. The reaction mixture was stirred vigorously at 120 °C for 1 day. After cooling to room temperature, it was poured into methanol (200 mL) and the precipitate was formed. The filtered polymer was then purified by Soxhlet extraction using methanol (1 d), acetone (1 d), hexane (1 d) and chloroform (1 d). The chloroform fraction was concentrated and re-precipitated in acetone, and dried in a high vacuum oven at room temperature.

PJ1. Isolated yield = 89%. ^{1}H NMR (400 MHz, CDCl$_3$, δ): 7.69 (s, 2H), 7.58 (s, 2H), 7.39 (s, 12H), 1.39–1.18 (br, 60H), 1.09–1.00(m, 18H), 0.96–0.81 (m, 24H). Anal. calcd for C$_{90}$H$_{135}$NO$_2$S$_7$Si$_2$: C,

70.03; H, 8.81; N, 0.91; S, 14.54. Found: C, 70.06; H, 9.24; N, 1.06; S, 14.38. M_n = 87.8 kDa, PDI = 1.58.

PJ2. Isolated yield = 75%. ^{1}H NMR (400 MHz, CDCl$_3$, δ): 7.77–7.40 (br, 6H), 7.21–6.78 (br, 4H), 3.50–3.11 (br, 4H), 1.88–0.57 (br, 72H). Anal. calcd for C$_{70}$H$_{88}$O$_2$S$_8$Si$_2$: C, 65.99; H, 6.96; S, 20.13. Found: C, 65.55; H, 6.95; S, 20.95. M_n = 80.1 kDa, PDI = 1.44.

PJ3. Isolated yield = 77%. ^{1}H NMR (400 MHz, CDCl$_3$, δ): 8.05–7.71 (br, 2H), 7.62–7.30 (br, 4H), 7.08–6.80 (br, 2H) 3.17–2.76 (br, 4H), 1.99–0.65 (br, 88H). Anal. calcd. for C$_{90}$H$_{134}$F$_2$N$_2$S$_7$Si$_2$: C, 69.17; H, 8.64; N, 1.79; S, 14.36. Found: C, 68.26; H, 8.36; N, 1.81; S, 14.28. M_n = 79.2 kDa, PDI = 1.56.

Synthesis of AIDIC

Synthesis of 4,4-dihexyl-6-(thiophen-2-yl)-4*H*-indeno[1,2-*b*]-thiophene (A2). Monomer A1 was prepared according to the previous reported procedure.[23] A suspension of monomer A1 (5 g, 19.7 mmol) and sodium *tert*-butoxide (9.13 g, 95.2 mmol) in 150 mL anhydrous DMSO was stirred at 80 °C for 1 h. 1-Bromohexane (13.4 mL, 95.2 mmol) was then added to the reaction mixture, and the resulting mixture was heated at 90 °C overnight. The reaction was quenched with water and extracted with chloroform. The organic layer was dried with MgSO$_4$ and the solvent removed under reduced pressure. The resulting crude mixture was purified by column chromatography (silica gel; eluent.: hexane) to give a yellow viscous oil (2.91 g, 35%). ^{1}H NMR (400 MHz, CDCl$_3$, δ): 7.54–7.50 (m, 2H), 7.38 (d, J = 8.0 Hz, 1H), 7.33 (q, J = 4.0 Hz, 1H), 7.31 (d, J = 4.0 Hz, 1H), 7.27–7.25 (m, 1H), 7.10–7.08 (m, 1H), 6.97 (d, J = 4.0 Hz, 1H), 2.00–1.83 (m, 4H), 1.19–1.03 (m, 12H), 0.91–0.85 (m, 4H), 0.80–0.74 (m, 6H). ^{13}C NMR (100 MHz, CDCl$_3$, δ): 155.98, 154.84, 145.39, 140.89, 137.94, 131.35, 128.14, 127.58, 124.93, 124.38, 122.71, 121.74, 120.19, 119.00, 54.17, 39.18, 31.69, 29.83, 24.27, 22.73, 14.17. Anal. calcd for C$_{27}$H$_{34}$S$_2$: C, 76.72; H, 8.11. Found: C, 76.62; H, 8.03.

Synthesis of 6-(5-formylthiophen-2-yl)-4,4-dihexyl-4*H*-indeno-[1,2-*b*]thiophene-2-carbaldehyde (A3). A Vilsmeier reagent, which was prepared with POCl$_3$ (0.5 mL) in DMF (10 mL), was added to a solution of monomer A2 (1.08 g, 2.56 mmol) in 1,2-dichloroethane (50 mL) under the protection of argon. The resulting mixture was stirred at 85 °C overnight, the reaction was quenched with water and then extracted with chloroform. The organic layer was dried with MgSO$_4$ and the solvent removed under reduced pressure. The resulting crude mixture was purified by column chromatography using hexane/ethyl acetate (9 : 1) as eluent., yielding a reddish viscous oil (0.82 g, 67%). ^{1}H NMR (400 MHz, CDCl$_3$, δ): 9.92 (d, J = 2.0 Hz, 2H), 7.77 (d, J = 4.0 Hz, 1H), 7.69–7.59 (m, 2H), 7.48 (d, J = 4 Hz, 1H), 2.06–1.87 (m, 4H), 1.18–1.06 (m, 12H), 0.91–0.81 (m, 4H), 0.80–0.77 (m, 6H). ^{13}C NMR (100 MHz, CDCl$_3$, δ): 183.18, 182.79, 156.48, 156.14, 154.23, 150.38, 146.48, 142.66, 138.02, 137.49, 132.44, 130.29, 126.05, 124.47, 121.33, 120.71, 54.74, 38.95, 31.59, 29.66, 24.35, 22.65, 14.09. Anal. calcd for C$_{29}$H$_{34}$O$_2$S$_2$: C, 72.76; H, 7.16. Found: C, 72.56; H, 7.23.

Synthesis of AIDIC. To a two-necked round-bottomed flask were added monomer A3 (0.2 g 0.42 mmol), 1,1-dicyanomethylene-3-indanone (0.62 g, 3.09 mmol), chloroform (50 mL), and pyridine (2 mL). The reaction mixture was stirred at 80 °C overnight.

This journal is © The Royal Society of Chemistry 2018

Energy Environ. Sci., 2018, **11**, 2569–2580 | **2577**

After cooling to room temperature, the volatile was removed under reduced pressure and then re-dissolved in 5 mL chloroform. The concentrated mixture was precipitated in methanol (200 mL) and filtered. The residue was purified by column chromatography using hexane/chloroform (4 : 1) as eluent., yielding a dark green solid (120 mg, 35%). ^{1}H NMR (400 MHz, CDCl$_3$): δ 9.00 (s, 1H), 8.92 (s, 1H), 8.73 (m, 2H), 8.00–7.95 (m, 3H), 7.91 (d, J = 4.0 Hz, 1H), 7.89–7.86 (m, 1H), 7.82–7.71 (m, 6H), 7.62 (d, J = 4 Hz, 1H), 2.14–1.92 (m, 4H), 1.19–1.05 (m, 12H), 0.91–0.85 (m, 4H), 0.80–0.76 (m, 6H). ^{13}C NMR (100 MHz, CDCl$_3$, δ): 188.56, 188.45, 160.74, 160.45, 159.69, 159.30, 157.44, 157.23, 146.26, 141.56, 141.26, 140.19, 140.09, 138.78, 138.73, 137.99, 137.97, 137.07, 135.57, 135.33, 134.88, 134.70, 133.73, 126.84, 125.60, 125.50, 125.26, 124.06, 123.96, 123.27, 122.48, 122.36, 122.31, 120.93, 114.85, 114.78, 114.53, 114.47, 70.47, 69.39, 54.97, 39.19, 31.68, 29.71, 24.50, 22.73, 14.14. Anal. calcd for C$_{53}$H$_{42}$N$_4$O$_2$S$_2$: C, 76.60; H, 5.09; N, 6.74. Found: C, 76.62; H, 5.01; N, 6.82.

Device fabrication and characterization

The NF-PSCs were fabricated with a configuration of ITO/PEDOT: PSS/active layer/PDINO/Al, where ITO, PEDOT:PSS, and PDINO refer to indium tin oxide, poly(3,4-ethylenedioxythiophene): poly(styrene sulfonate), and perylene diimide functionalized with amino N-oxide, respectively. PEDOT:PSS (Bayer Baytron 4083) was spin-coated at 4000 rpm onto the ITO substrate, followed by annealing at 140 °C for 20 min in air. The active layer was spin-coated from CF/DIO (v/v = 1/0.5 vol%) solutions with a donor/acceptor weight ratio of 1 : 1.5 wt%, followed by a thermal annealing treatment at 130 °C for 5 min. Then methanol solution of PDINO (1.0 mg mL^{-1}) was then deposited onto the active layer with a spin rate of 3000 rpm for 60 s. Finally, 100 nm aluminum was thermally evaporated under vacuum ($<$5.0 $\times$ 10^{-5} Pa). The active area of each sample was 13.0 mm^2. The current density $versus$ voltage (J–V) characteristics were recorded using a Keithley 2400 source under illumination of an AM 1.5G solar simulator with an intensity of 100 mW cm^{-2}. The external quantum efficiency (EQE) measurements were conducted using Model QEX7 by PV measurements Inc. (Boulder, Colorado) in ambient air. The thickness of the active layers was measured using a stylus profilometer (P6, KLA Tencor). The hole and electron mobilities were measured via using the space charge limited current (SCLC) method.[65] Device structures are ITO/PEDOT:PSS/active layer/ Au for hole-only devices and ITO/ZnO/active layer/PDINO/Al for electron-only devices, respectively. The SCLC mobilities were calculated using the Mott–Gurney equation:

$$J = \frac{9\varepsilon_r \varepsilon_0 \mu V^2}{8L^3} \qquad (1)$$

where ε_r is the relative dielectric constant of the organic semiconductor, ε_0 is the permittivity of empty space, μ is the mobility of zero-field, L is the thickness of the active layer, and V = $V_{applied}$ − $V_{built-in}$ − $V_{series-resistance}$ (the V_{bi} values are 0.2 V and 0 V for the hole-only and the electron-only devices, respectively), where $V_{applied}$ is the voltage applied, and $V_{built-in}$ is the built-in voltage from the relative work function difference between the two electrodes. $V_{series-resistance}$ is the voltage caused by the series and contact resistance potential drop ($V_{series-resistance}$ = J $\times$ $R_{series-resistance}$). For convenience, the voltage drops caused by this resistance ($R_{series-resistance}$) was ignored.

Morphology characterization

The atomic force spectroscopy (AFM) images of blend films were recorded using the Agilent 5500 scanning probe microscope (SPM) running with a Nano scope V controller. The scanning transmission electron microscopy (STEM) analysis was conducted using a JEOL USA JEM-2100F (Cs corrector) transmission electron microscope. The GIWAXS measurement was carried out at the PLS-II 6A U-SAXS beamline of the Pohang Accelerator Laboratory in Korea. The X-rays coming from the in-vacuum undulator (IVU) were monochromated (wavelength λ = 1.10994 Å) using a double crystal monochromator and focused both horizontally and vertically (450 (H) $\times$ 60 (V) μm^2 in FWHM @ the sample position) using K-B type mirrors. The grazing incidence wide-angle X-ray scattering (GIWAXS) sample stage was equipped with a 7-axis motorized stage for the fine alignment of the sample, and the incidence angles of the X-ray beam were set to be 0.11°–0.13° for the neat and blend films. The GIWAXS patterns were recorded with a 2D CCD detector (Rayonix SX165) and an X-ray irradiation time within 100 s, dependent on the saturation level of the detector. Diffraction angles were calibrated using a sucrose standard (monoclinic, $P21$, a = 10.8631 Å, b = 8.7044 Å, c = 7.7624 Å, and β = 102.938°) and the sample-to-detector distance was $\sim$231 mm.

Conflicts of interest

There are no conflicts to declare.

Acknowledgements

Notes and references

1 C. B. Nielsen, S. Holliday, H. Y. Chen, S. J. Cryer and I. McCulloch, *Acc. Chem. Res.*, 2015, **48**, 2803–2812.
2 S. Li, L. Ye, W. Zhao, S. Zhang, H. Ade and J. Hou, *Adv. Energy Mater.*, 2017, **7**, 1700183.
3 S. Li, L. Ye, W. Zhao, S. Zhang, S. Mukherjee, H. Ade and J. Hou, *Adv. Mater.*, 2016, **28**, 9423–9429.
4 W. Gao, Q. An, R. Ming, D. Xie, K. Wu, Z. Luo, Y. Zou, F. Zhang and C. Yang, *Adv. Funct. Mater.*, 2017, **27**, 1702194.
5 C. Zhan and J. Yao, *Chem. Mater.*, 2016, **28**, 1948–1964.
6 W. Zhao, S. Li, H. Yao, S. Zhang, Y. Zhang, B. Yang and J. Hou, *J. Am. Chem. Soc.*, 2017, **139**, 7148–7151.
7 N. Liang, W. Jiang, J. Hou and Z. Wang, *Mater. Chem. Front.*, 2017, **1**, 1291–1303.
8 S. Li, Z. Zhang, M. Shi, C. Z. Li and H. Chen, *Phys. Chem. Chem. Phys.*, 2017, **19**, 3440–3458.

9 C. Zhan, X. Zhang and J. Yao, *RSC Adv.*, 2015, **5**, 93002–93026.

10 S. Li, W. Liu, C. Z. Li, M. Shi and H. Chen, *Small*, 2017, **13**, 1701120.

11 H. Fu, Z. Wang and Y. Sun, *Sol. RRL*, 2018, **2**, 1700158.

12 D. Baran, T. Kirchartz, S. Wheeler, S. Dimitrov, M. Abdelsamie, J. Gorman, R. S. Ashraf, S. Holliday, A. Wadsworth, N. Gasparini, P. Kaienburg, H. Yan, A. Amassian, C. J. Brabec, J. R. Durrant and I. McCulloch, *Energy Environ. Sci.*, 2016, **9**, 3783–3793.

13 S. Dai, F. Zhao, Q. Zhang, T. K. Lau, T. Li, K. Liu, Q. Ling, C. Wang, X. Lu, W. You and X. Zhan, *J. Am. Chem. Soc.*, 2017, **139**, 1336–1343.

14 F. Zhao, S. Dai, Y. Wu, Q. Zhang, J. Wang, L. Jiang, Q. Ling, Z. Wei, W. Ma, W. You, C. Wang and X. Zhan, *Adv. Mater.*, 2017, **29**, 1700144.

15 Q. Fan, Y. Wang, M. Zhang, B. Wu, X. Guo, Y. Jiang, W. Li, B. Guo, C. Ye, W. Su, J. Fang, X. Ou, F. Liu, Z. Wei, T. C. Sum, T. P. Russell and Y. Li, *Adv. Mater.*, 2018, **30**, 1704546.

16 Y. Lin, J. Wang, Z. G. Zhang, H. Bai, Y. Li, D. Zhu and X. Zhan, *Adv. Mater.*, 2015, **27**, 1170–1174.

17 J. Wang, W. Wang, X. Wang, Y. Wu, Q. Zhang, C. Yan, W. Ma, W. You and X. Zhan, *Adv. Mater.*, 2017, **29**, 1702125.

18 S. Holliday, R. S. Ashraf, C. B. Nielsen, M. Kirkus, J. A. Rohr, C. H. Tan, E. Collado-Fregoso, A. C. Knall, J. R. Durrant, J. Nelson and I. McCulloch, *J. Am. Chem. Soc.*, 2015, **137**, 898–904.

19 Y. Lin, F. Zhao, Q. He, L. Huo, Y. Wu, T. C. Parker, W. Ma, Y. Sun, C. Wang, D. Zhu, A. J. Heeger, S. R. Marder and X. Zhan, *J. Am. Chem. Soc.*, 2016, **138**, 4955–4961.

20 N. D. Eastham, A. S. Dudnik, T. J. Aldrich, E. F. Manley, T. J. Fauvell, P. E. Hartnett, M. R. Wasielewski, L. X. Chen, F. S. Melkonyan, A. Facchetti, R. P. H. Chang and T. J. Marks, *Chem. Mater.*, 2017, **29**, 4432–4444.

21 S. V. Gupta, A. Bagui and S. P. Singh, *Adv. Funct. Mater.*, 2017, **27**, 1603820.

22 J. E. Anthony, A. Facchetti, M. Heeney, S. R. Marder and X. Zhan, *Adv. Mater.*, 2010, **22**, 3876–3892.

23 S. Holliday, R. S. Ashraf, A. Wadsworth, D. Baran, S. A. Yousaf, C. B. Nielsen, C. H. Tan, S. D. Dimitrov, Z. Shang, N. Gasparini, M. Alamoudi, F. Laquai, C. J. Brabec, A. Salleo, J. R. Durrant and I. McCulloch, *Nat. Commun.*, 2016, **7**, 11585.

24 F. Liu, T. Hou, X. Xu, L. Sun, J. Zhou, X. Zhao and S. Zhang, *Macromol. Rapid Commun.*, 2018, **39**, 1700555.

25 Z. Li, K. Jiang, G. Yang, J. Y. Lai, T. Ma, J. Zhao, W. Ma and H. Yan, *Nat. Commun.*, 2016, **7**, 13094.

26 T. Yu, X. Xu, G. Zhang, J. Wan, Y. Li and Q. Peng, *Adv. Funct. Mater.*, 2017, **27**, 1701491.

27 H. Yao, Y. Li, H. Hu, P. C. Y. Chow, S. Chen, J. Zhao, Z. Li, J. H. Carpenter, J. Y. L. Lai, G. Yang, Y. Liu, H. Lin, H. Ade and H. Yan, *Adv. Energy Mater.*, 2018, **8**, 1701895.

28 Z. Zheng, O. M. Awartani, B. Gautam, D. Liu, Y. Qin, W. Li, A. Bataller, K. Gundogdu, H. Ade and J. Hou, *Adv. Mater.*, 2017, **29**, 1604241.

29 S. Li, L. Ye, W. Zhao, X. Liu, J. Zhu, H. Ade and J. Hou, *Adv. Mater.*, 2017, **29**, 1704051.

30 L. Xue, Y. Yang, J. Xu, C. Zhang, H. Bin, Z. G. Zhang, B. Qiu, X. Li, C. Sun, L. Gao, J. Yao, X. Chen, Y. Yang, M. Xiao and Y. Li, *Adv. Mater.*, 2017, **29**, 1703344.

31 H. Yao, L. Ye, J. Hou, B. Jang, G. Han, Y. Cui, G. M. Su, C. Wang, B. Gao, R. Yu, H. Zhang, Y. Yi, H. Y. Woo, H. Ade and J. Hou, *Adv. Mater.*, 2017, **29**, 1700254.

32 H. Bin, L. Gao, Z. G. Zhang, Y. Yang, Y. Zhang, C. Zhang, S. Chen, L. Xue, C. Yang, M. Xiao and Y. Li, *Nat. Commun.*, 2016, **7**, 13651.

33 W. Zhao, D. Qian, S. Zhang, S. Li, O. Inganas, F. Gao and J. Hou, *Adv. Mater.*, 2016, **28**, 4734–4739.

34 D. Baran, R. S. Ashraf, D. A. Hanifi, M. Abdelsamie, N. Gasparini, J. A. Rohr, S. Holliday, A. Wadsworth, S. Lockett, M. Neophytou, C. J. Emmott, J. Nelson, C. J. Brabec, A. Amassian, A. Salleo, T. Kirchartz, J. R. Durrant and I. McCulloch, *Nat. Mater.*, 2017, **16**, 363–369.

35 Y. Lin, F. Zhao, Y. Wu, K. Chen, Y. Xia, G. Li, S. K. Prasad, J. Zhu, L. Huo, H. Bin, Z. G. Zhang, X. Guo, M. Zhang, Y. Sun, F. Gao, Z. Wei, W. Ma, C. Wang, J. Hodgkiss, Z. Bo, O. Inganas, Y. Li and X. Zhan, *Adv. Mater.*, 2017, **29**, 1604155.

36 Y. Lin, T. Li, F. Zhao, L. Han, Z. Wang, Y. Wu, Q. He, J. Wang, L. Huo, Y. Sun, C. Wang, W. Ma and X. Zhan, *Adv. Energy Mater.*, 2016, **6**, 1600854.

37 J. Zhang, K. Jiang, G. Yang, T. Ma, J. Liu, Z. Li, J. Y. L. Lai, W. Ma and H. Yan, *Adv. Energy Mater.*, 2017, 1602119, DOI: 10.1002/aenm.201602119,.

38 H. Hu, K. Jiang, P. C. Y. Chow, L. Ye, G. Zhang, Z. Li, J. H. Carpenter, H. Ade and H. Yan, *Adv. Energy Mater.*, 2018, **8**, 1701674.

39 S. Chen, H. J. Cho, J. Lee, Y. Yang, Z.-G. Zhang, Y. Li and C. Yang, *Adv. Energy Mater.*, 2017, **7**, 1701125.

40 D. M. Stoltzfus, J. E. Donaghey, A. Armin, P. E. Shaw, P. L. Burn and P. Meredith, *Chem. Rev.*, 2016, **116**, 12920–12955.

41 A. J. Heeger, *Adv. Mater.*, 2014, **26**, 10–27.

42 J. D. Douglas, M. S. Chen, J. R. Niskala, O. P. Lee, A. T. Yiu, E. P. Young and J. M. Frechet, *Adv. Mater.*, 2014, **26**, 4313–4319.

43 Y. Fang, A. K. Pandey, A. M. Nardes, N. Kopidakis, P. L. Burn and P. Meredith, *Adv. Energy Mater.*, 2013, **3**, 54–59.

44 S. Chen, Y. Liu, L. Zhang, P. C. Y. Chow, Z. Wang, G. Zhang, W. Ma and H. Yan, *J. Am. Chem. Soc.*, 2017, **139**, 6298–6301.

45 J. Liu, S. Chen, D. Qian, B. Gautam, G. Yang, J. Zhao, J. Bergqvist, F. Zhang, W. Ma, H. Ade, O. Inganäs, K. Gundogdu, F. Gao and H. Yan, *Nat. Energy*, 2016, **1**, 16089.

46 H. Bin, Y. Yang, Z. Peng, L. Ye, J. Yao, L. Zhong, C. Sun, L. Gao, H. Huang, X. Li, B. Qiu, L. Xue, Z.-G. Zhang, H. Ade and Y. Li, *Adv. Energy Mater.*, 2018, **8**, 1702324.

47 M. Wang, D. Cai, Z. Yin, S. C. Chen, C. F. Du and Q. Zheng, *Adv. Mater.*, 2016, **28**, 3359–3365.

48 Z.-G. Zhang, B. Qi, Z. Jin, D. Chi, Z. Qi, Y. Li and J. Wang, *Energy Environ. Sci.*, 2014, **7**, 1966.

49 H. Yao, Y. Chen, Y. Qin, R. Yu, Y. Cui, B. Yang, S. Li, K. Zhang and J. Hou, *Adv. Mater.*, 2016, **28**, 8283–8287.

50 R. Yu, S. Zhang, H. Yao, B. Guo, S. Li, H. Zhang, M. Zhang and J. Hou, *Adv. Mater.*, 2017, **29**, 1700437.

51 B. Fan, W. Zhong, X.-F. Jiang, Q. Yin, L. Ying, F. Huang and Y. Cao, *Adv. Energy Mater.*, 2017, **7**, 1602127.

52 T. Zhang, X. Zhao, D. Yang, Y. Tian and X. Yang, *Adv. Energy Mater.*, 2018, **8**, 1701691.

This journal is © The Royal Society of Chemistry 2018

Energy Environ. Sci., 2018, **11**, 2569–2580 | 2579

53 G. Zhang, G. Yang, H. Yan, J. H. Kim, H. Ade, W. Wu, X. Xu, Y. Duan and Q. Peng, *Adv. Mater.*, 2017, **29**, 1606054.

54 T. Kumari, S. M. Lee, S.-H. Kang, S. Chen and C. Yang, *Energy Environ. Sci.*, 2017, **10**, 258–265.

55 H. Bin, Y. Yang, Z. G. Zhang, L. Ye, M. Ghasemi, S. Chen, Y. Zhang, C. Zhang, C. Sun, L. W. Xue, C. Yang, H. Ade and Y. Li, *J. Am. Chem. Soc.*, 2017, **139**, 5085–5094.

56 H. Hu, P. C. Y. Chow, G. Zhang, T. Ma, J. Liu, G. Yang and H. Yan, *Acc. Chem. Res.*, 2017, **50**, 2519–2528.

57 T. Kim, J. H. Kim, T. E. Kang, C. Lee, H. Kang, M. Shin, C. Wang, B. Ma, U. Jeong, T. S. Kim and B. J. Kim, *Nat. Commun.*, 2015, **6**, 8547.

58 H. Kang, K.-H. Kim, J. Choi, C. Lee and B. J. Kim, *ACS Macro Lett.*, 2014, **3**, 1009–1014.

59 Y. J. Hwang, T. Earmme, B. A. Courtright, F. N. Eberle and S. A. Jenekhe, *J. Am. Chem. Soc.*, 2015, **137**, 4424–4434.

60 H. Kang, M. A. Uddin, C. Lee, K. H. Kim, T. L. Nguyen, W. Lee, Y. Li, C. Wang, H. Y. Woo and B. J. Kim, *J. Am. Chem. Soc.*, 2015, **137**, 2359–2365.

61 Z. Li, X. Xu, W. Zhang, X. Meng, W. Ma, A. Yartsev, O. Inganas, M. R. Andersson, R. A. Janssen and E. Wang, *J. Am. Chem. Soc.*, 2016, **138**, 10935–10944.

62 N. Zhou, A. S. Dudnik, T. I. Li, E. F. Manley, T. J. Aldrich, P. Guo, H. C. Liao, Z. Chen, L. X. Chen, R. P. Chang, A. Facchetti, M. Olvera de la Cruz and T. J. Marks, *J. Am. Chem. Soc.*, 2016, **138**, 1240–1251.

63 X. Guo, N. Zhou, S. J. Lou, J. Smith, D. B. Tice, J. W. Hennek, R. P. Ortiz, J. T. L. Navarrete, S. Li, J. Strzalka, L. X. Chen, R. P. H. Chang, A. Facchetti and T. J. Marks, *Nat. Photonics*, 2013, **7**, 825–833.

64 D. Bartesaghi, C. Perez Idel, J. Kniepert, S. Roland, M. Turbiez, D. Neher and L. J. Koster, *Nat. Commun.*, 2015, **6**, 7083.

65 P. Schilinsky, C. Waldauf and C. J. Brabec, *Appl. Phys. Lett.*, 2002, **81**, 3885–3887.

66 S. R. Cowan, A. Roy and A. J. Heeger, *Phys. Rev. B: Condens. Matter Mater. Phys.*, 2010, **82**, 245207.

67 M. Lenes, M. Morana, C. J. Brabec and P. W. M. Blom, *Adv. Funct. Mater.*, 2009, **19**, 1106–1111.

68 S. M. Menke and R. J. Holmes, *Energy Environ. Sci.*, 2014, **7**, 499–512.

69 C. M. Proctor, M. Kuik and T.-Q. Nguyen, *Prog. Polym. Sci.*, 2013, **38**, 1941–1960.

70 H. J. Cho, Y. J. Kim, S. Chen, J. Lee, T. J. Shin, C. E. Park and C. Yang, *Nano Energy*, 2017, **39**, 229–237.

2580 | *Energy Environ. Sci.*, 2018, **11**, 2569–2580

This journal is © The Royal Society of Chemistry 2018